Title

Durability of symmetric-structured metal-supported solid oxide fuel cells

Author

Tucker, Michael C

Publication Date

2017-11-01

DOI

10.1016/j.jpowsour.2017.09.075

Durability of Symmetric-Structured Metal-Supported Solid Oxide Fuel Cells

Michael C. Tucker*

Energy Conversion Group, Energy Technologies Area

Lawrence Berkeley National Laboratory

1 Cyclotron Rd

Berkeley, CA 94720 USA

Abstract

Symmetric-structure metal-supported solid oxide fuel cells (MS-SOFC) with YSZ electrolyte are fabricated with porous YSZ backbone electrodes, stainless steel supports, and infiltrated catalysts on both anode and cathode side. Durability towards aggressive thermal and redox cycling, and long-term operation is assessed. Many sealing material candidates are screened for compatibility with the cell materials and operating conditions, and a commercial sealing glass, GM31107, is selected. LSM/SDCN cells are then subjected to 200 very fast thermal cycles and 20 complete redox cycles, with minimal impact to cell performance. LSM/SDCN and SDCN/SDCN cells are operated for more than 1200 h at 700°C. The seal and cell hermeticity is maintained, and cell ohmic impedance does not change significantly during operation. Electrode polarization increases during operation, leading to significant degradation of the cell performance. In-operando EIS and post-mortem SEM/EDS analysis suggest that catalyst coarsening and cathode Cr deposition are the dominant degradation modes.

*mctucker@lbl.gov

Phone 1-510-486-5304

Fax 1-510-486-4260

LBNL; 1 Cyclotron Rd; MS 70-108B; Berkeley CA 94720; USA

1. Introduction

Metal-supported solid oxide fuel cells (MS-SOFC) display a number of advantages over conventional anode-supported (ASC) and electrolyte-supported (ESC) SOFCs, including low-cost structural materials (e.g. stainless steel), mechanical ruggedness, excellent tolerance to redox cycling, and extremely fast start-up capability. Challenges for MS-SOFCs include: oxidation of the metal support, especially at 800°C and higher; fabrication and materials set restrictions arising from the requirement that stainless steel be sintered in reducing atmosphere; and, performance and lifetime are typically well below the best achievements of all-ceramic SOFCs. These issues, and various approaches to overcome the challenges, have been discussed in detail in the literature [1–5].

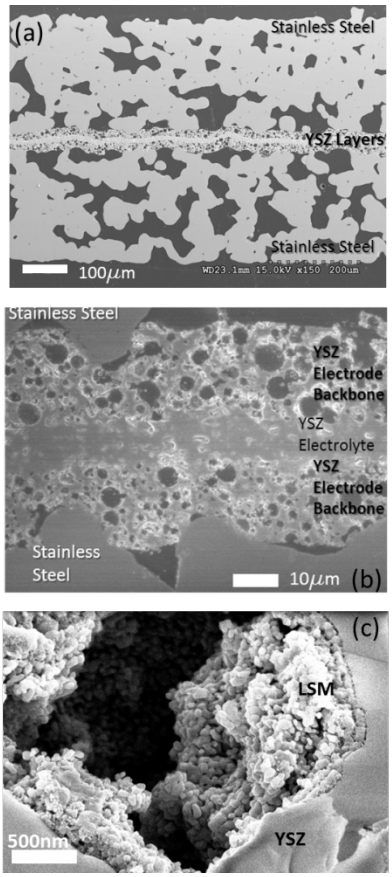

Figure 1. SEM image of (a,b) polished cross section of MS-SOFC structure after sintering and before catalyst infiltration, and (c) cathode pore after infiltration of LSM. Reproduced with permission from Ref. 9.

The majority of global MS-SOFC development focuses on cell architectures supported by a single stainless steel layer on the anode side [1,2,5]. This enables the use of conventional cathode catalysts and structures, as well as conventional stainless steel bipolar plates with Cr-migration barrier layer. Furthermore, it avoids intimate contact between the cathode and bare stainless steel, for which accelerated Cr deposition in the cathode would be a concern. Recently, MS-SOFCs with the cathode instead applied to a presintered stainless steel substrate by plasma spray deposition have been investigated; this avoids interdiffusion between Fe and Cr from the stainless steel and Ni from the anode [6,7].

Lawrence Berkeley National Laboratory (LBNL) has developed an alternative cell architecture with metal supports on both the anode and cathode sides, shown in Figure 1 [8–10]. The benefits of this design include: efficient current collection on both sides; ability to weld electrical interconnections to both sides; mechanical ruggedness; and, high power density. Furthermore, the symmetric backbone architecture means that mismatch between the sintering profiles or thermal expansion coefficients of the ceramic and metal layers does not produce cell warping. This cell architecture has proven to be particularly tolerant to extremely rapid thermal cycling, in which the cell is heated to operating temperature within 20 seconds by direct flame impingement [11]. The use of metal support on both sides is enabled by infiltration of both the anode and cathode catalysts. Both catalysts are introduced after high-temperature reducing atmosphere sintering is completed, and therefore do not react with the cell backbone materials. The low catalyst processing temperature furthermore provides nano-scale catalyst particles, leading to high power density as we reported recently for cells with the anode infiltrated with a mixture of samaria-doped ceria and nickel (SDCN), and the cathode infiltrated with either lanthanum strontium manganese oxide (LSM), or SDCN [9]. In the case that the same catalyst is used on both anode and cathode sides, a fully symmetric cell is obtained. This approach makes infiltration simpler (the cell can be dunked in a precursor bath without any masking) and removes the need for tracking which side of the cell is which during stack assembly. Symmetric cells with SDCN catalyst were used at Point Source Power to overcome rapid degradation observed for LSM cathode via Cr contamination in the presence of K-containing biomass fuel

[12–14]. A fully symmetric cell also enables innovative applications and operating strategies proposed in the literature [15,16].

MS-SOFCs with the metal support on only the anode side have been operated for 2000 and 3000 h with YSZ electrolyte [17,18] and 2000 h with CGO electrolyte [19]. In contrast, only short-term stability up to a few hundred hours has been demonstrated for MS-SOFCs with metal supports on both sides [1,8,20]. In this paper, we report for the first time >1200 h operation of MS-SOFCs with metal supports on both sides, and begin to elucidate the dominant degradation modes. Tolerance to rapid thermal cycling and redox cycling is also assessed.

2. Experimental Methods

Green cells were assembled by laminating individual YSZ (8Y, Tosoh) or stainless steel (P434L alloy, water atomized, Ametek Specialty Metal Products) layers prepared by tape-casting. The layers were prepared with polymethyl methacrylate poreformer beads (Esprix Technologies) and water-based tape-casting binder. Individual cells were cut from a larger green sheet with a laser cutter (Hobby model, Full Spectrum Laser). Cells were then debinded by firing in air in a box furnace at 525°C for 1 h with 0.5°C min^{-1} heat-up rate to slowly remove the binder and poreformer. Cells were sintered at 1350°C for 2h in a tube furnace with flowing 2% hydrogen in argon. Sintered cells were circular with a diameter of 30mm.

After sintering, cells were infiltrated by techniques described previously with $La_{0.15}Sr_{0.85}MnO_{3-\delta}$ (LSM) on the cathode side and 80 v% $Sm_{0.2}Ce_{0.8}O_{2-\delta}$-20 v% Ni (SDCN) on the anode side [9,10,21]. Fully-symmetric cells were also fabricated with SDCN on both sides. Precursor mixtures of metal nitrates (Sigma Aldrich) were prepared with the intended final stoichiometric composition, with Triton-X surfactant (Sigma Aldrich, at surfactant loading of 0.3 g per 2 g of resulting catalyst particles) and water added to improve wetting into the cell pores (20w% for LSM, 40w% for SDCN). The precursor mixture

was heated to ~90°C, the cell was submerged into it, and then mild vacuum was applied to evacuate the cell pores. Areas of the cell that were not intended to be infiltrated were coated with acrylic paint mask (Liquitex) to make a 1 cm^2 active area. After introducing the precursor into the cell, it was fired to 850°C in air to convert the precursor to the intended oxide phases. Any loose catalyst was removed from the surface of the cell by light brushing. Cells were re-infiltrated two additional times (and heated to only 600°C during these infiltration steps) before operation and testing. This infiltration heating protocol is tailored for high power density, as discussed in Reference [9].

Complete cells were mounted to a 410 stainless steel test rig using GM31107 (Schott) sealing glass. Further information on the selection of this glass seal material is available in Supplementary Information and Ref. [22]. Note that this glass does not contain Na or K, which are known to promote accelerated Cr deposition in the cathode [23].Each side of the cell was contacted with two NiCr wires, attached with a small piece of platinum mesh spot-welded to the wire and the cell. Glass paste consisting of glass powder mixed with terpineol ink vehicle (Fuel Cell Materials) was applied to the edge of the cell and adjoining surface of the test rig with a syringe. Cells were heated at 2°C min^{-1} to 200°C to remove the ink vehicle and then 10°C min^{-1} to 700°C and held for one hour with ambient air on both sides of the cell for glass sealing. The anode chamber was then flushed with nitrogen followed by hydrogen bubbled through water at room temperature flowing at 120 cm^3 min^{-1} at standard conditions. Open circuit voltage (OCV), current-step I-V polarization, and electrochemical impedance spectroscopy (EIS) (at OCV, 200 kHz to 0.1 Hz) were recorded with a multichannel potentiostat and current booster (Biologic).

Thermal cycling was accomplished by leaving the test rig and cell in a clam-shell tube furnace and adjusting the furnace temperature. The furnace was cooled naturally (initial cooling rate ~10° C min^{-1}), followed by heating at full furnace power, which took 15 min to reach 700°C. Redox cycling was accomplished by switching the anode gas between air and hydrogen at 700°C holding each for 6 min,

with a 2 min nitrogen flush between each step. All gas flow rates were 150 cm^3 min^{-1}. The anode chamber and inlet manifold volumes of the test rig are approximately 1 and 12 cm^3, respectively, so complete flushing by each new gas is expected within seconds. Tracking the OCV and impedance of the cell indicated that complete oxidation and reduction of the anode occurred within seconds, although each gas was held for a few minutes to ensure steady-state conditions. For comparison, a commercial anode-supported cell (MSRI) was also subjected to redox cycling.

Long-term operation was conducted by holding the cell isothermally at 0.7V and monitoring current. Under these conditions, fuel utilization was in the range 2 to 6%. Occasionally the voltage hold was interrupted briefly to assess OCV, impedance, and polarization performance. After long-term operation, post-mortem observations were made after delaminating the metal and ceramic layers with a sharp knife. The metal was mounted in epoxy (Struers), cross-sectioned with a wafering blade, and polished. The ceramic layers were fractured to provide a cross-section surface for analysis. Scanning electron microscope (SEM) and energy dispersive spectroscopy (EDS) analysis was carried out using a field-emission microscope (Zeiss Gemini Ultra-55).

3. Results and Discussion

3.1 Thermal and Redox Cycling

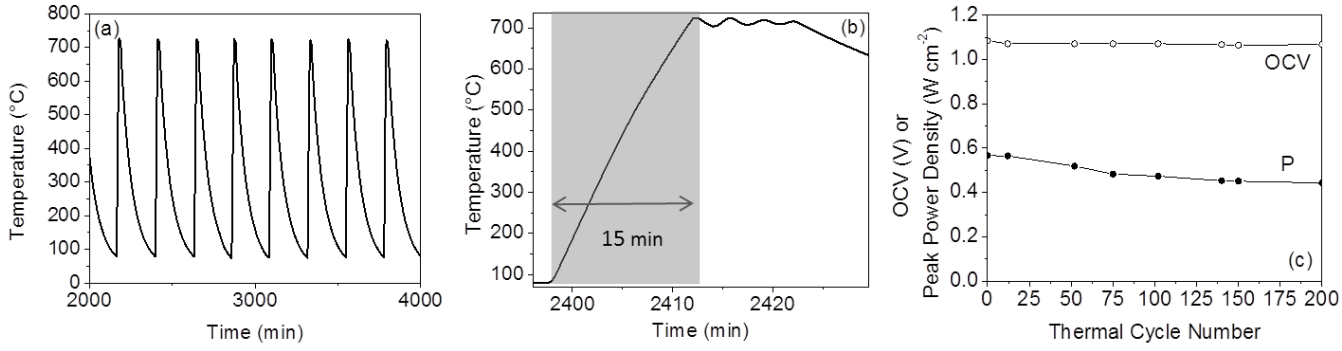

Figure 2. Rapid thermal cycling of LSM/SDCN cell. Temperature history for (a) several cycles and (b) a

single heat-up. (c) Cell OCV (open symbols) and peak power density (closed symbols) at 700°C during repeated thermal cycling.

The choice of cell backbone materials, seal, and test rig material with similar coefficients of thermal expansion allows for rapid thermal cycling without cell warping or seal cracking. Furthermore, the mechanical ruggedness of the MS-SOFC enables it to tolerate rapid thermal transients that can lead to failure of anode-supported cells (ASCs) [24], although under favorable conditions, successful startup of small ASCs in a few minutes has been reported [25]. A MS-SOFC was cycled 200 times between 80 and 700°C, with 15 min heat-up (average 41°C min^{-1} heating rate) as shown in Figure 2. The OCV remained stable, indicating integrity of the cell and seal. The MS-SOFC peak power density declined 22%, although we assign approximately half this degradation to cumulative exposure to the operating temperature, as opposed to arising from thermal cycling specifically. In particular, the cell experienced approximately 65 h above 600°C during the 200 thermal cycles, and this can be compared to the 10 and 12% degradation in current density observed over the first 65 h of continuous operation at 650 and 700°C, respectively (see Figure 4). The thermal cycling tolerance of MS-SOFC observed here is consistent with previous reports, although the number of cycles, heating rate, and temperature range used here is among the most aggressive to date [8,11,26,27].

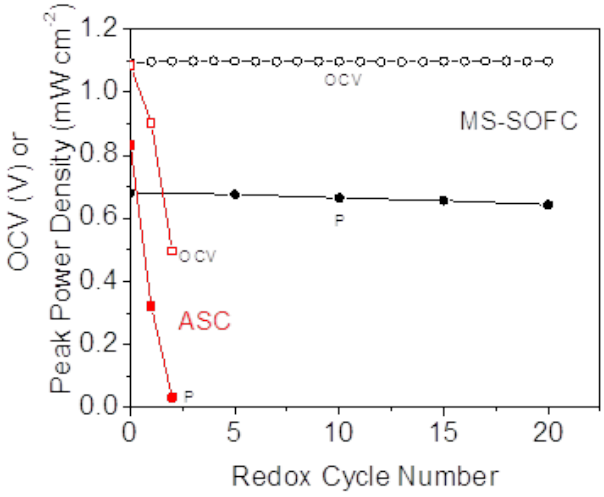

Figure 3. Deep redox cycling of LSM/SDCN MS-SOFC cell (black) and ASC (red). Cell OCV (open symbols) and peak power density (closed symbols) at 700°C during repeated air/hydrogen redox cycling of the anode.

Oxidation of the anode catalyst is expected in the event of cooling without blanketing gas, unintended loss of fuel supply, or spatially non-uniform fuel composition or current density conditions especially during operational transients. Oxidation of Ni to NiO in a conventional ASC leads to a large volume expansion of the anode and exerts significant stress on the electrolyte membrane, causing catastrophic failure in just a few oxidation/reduction (redox) cycles [8,28]. In contrast, the MS-SOFC architecture used here does not contain Ni in the mechanical backbone of the cell. Small Ni particles decorate the YSZ backbone, but these can expand and contract without causing any stress to the electrode backbone or electrolyte membrane. The MS-SOFC anode was cycled between hydrogen and air 20 times, with complete oxidation and reduction of the Ni occurring on each cycle. As shown in Figure 3, the cell survived with minimal impact to the performance or sealing. In contrast, a commercial ASC button cell subjected to the same deep redox cycling cracked and completely failed in the first 3 cycles. Furthermore, the MS-SOFC has the additional benefit of completing anode reduction within a matter of seconds after exposure to hydrogen, whereas the ASC required several hours for complete conversion of NiO to Ni.

The proven ability to heat up rapidly and tolerate intermittent fuel supply is expected to be a key benefit of MS-SOFCs for various non-baseload applications, including portable power generators, backup generators, and automotive auxiliary power and range extender units.

3.2 Long-term operation

Temperature-dependence of the initial performance for this MS-SOFC design was reported previously in the range 600 to 800°C, and scaled linearly from 0.44 to 1.9 W cm^{-2} [9]. Here, MS-SOFCs are operated for 200 to 300 h to assess initial stability at various temperatures. As shown in Figure 4, the cell operated

at 750°C degraded rapidly, whereas operation at 650 and 700°C was more stable. This is not surprising, as both catalyst coarsening and Cr deposition in the cathode are expected to increase significantly with temperature. Note that in all cases, the seal was maintained as indicated by the stable OCV data in Figure 4b, so degradation must be attributed to cell evolution. Because of the rapid degradation at 750°C and the lower performance at 650°C, 700°C was chosen as the temperature for long-term durability testing.

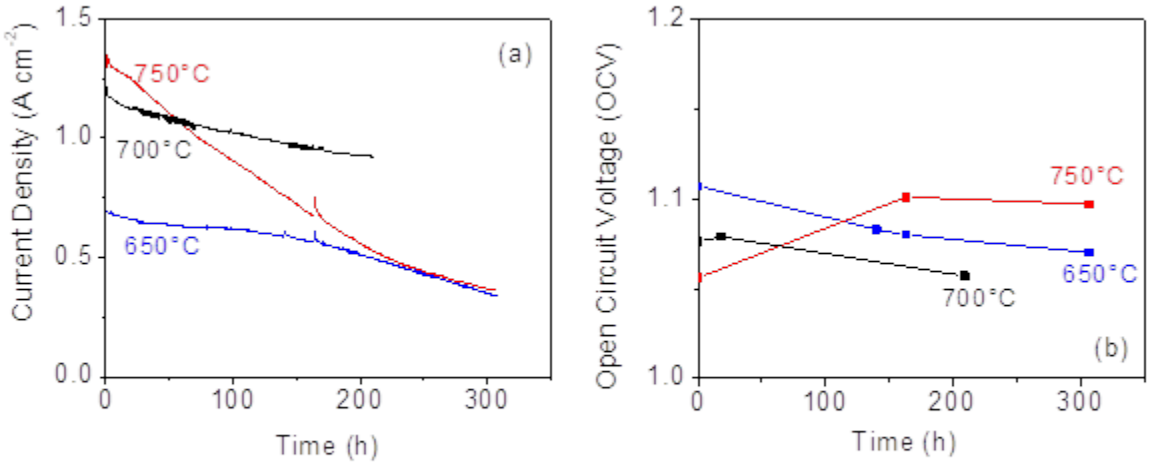

Figure 4. Temperature-dependence of the initial cell stability of LSM/SDCN cell. (a) Current density at 0.7 V and (b) OCV for cells operated potentiostatically at 650°C (blue), 700°C (black) and 750°C (red).

MS-SOFCs with LSM cathode and symmetric SDCN catalysts were operated at 700°C and 0.7 V for more than 1200 h, as shown in Figure 5a. This is by far the longest operation time reported to date for cells with metal supports on both sides [1,5,8,20].The LSM/SDCN cell shows relatively rapid degradation at the beginning of operation, and the cell becomes somewhat more stable as operation continues. For the SDCN/SDCN symmetric cell, after about 200 h the cell degrades linearly, at a lower rate than the LSM/SDCN. The average power density degradation rates over the entire testing time were 60%/kh for LSM/SDCN and 54%/kh for SDCN/SDCN. This suggests that the SDCN cathode is more stable than LSM under these conditions because both cells have identical anodes; although the initial performance of

the SDCN/SDCN cell is about half that of the LSM/SDCN cell, at the end of operation both cells give similar performance. Note that the initial transient during the first 200 h for SDCN/SDCN was observed in multiple cells, however, at this point no clear explanation can be offered.

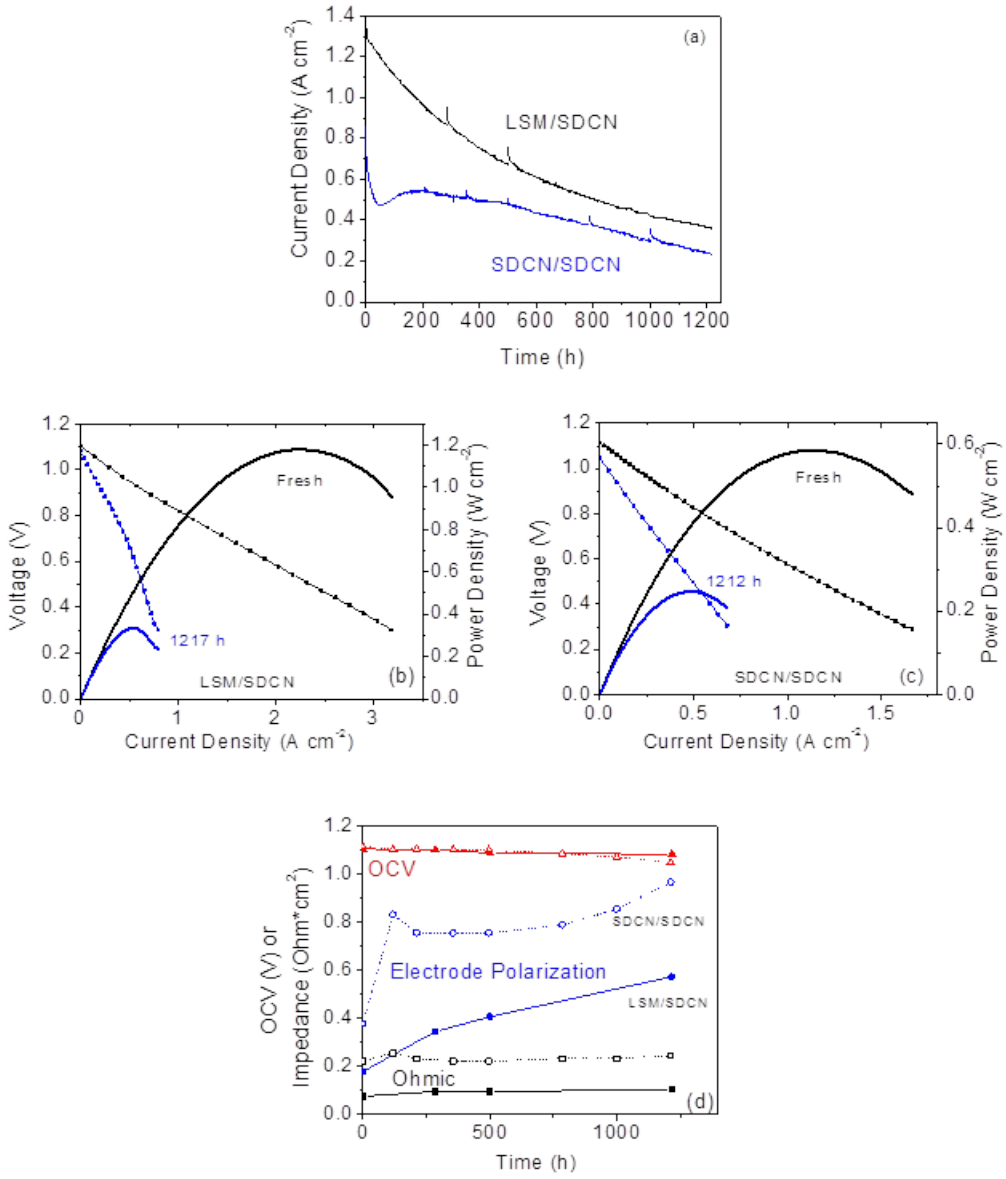

Figure 5. Long-term operation. (a) Current density at 0.7 V for cells operated potentiostatically at 700°C with LSM/SDCN (black) and symmetric SDCN/SDCN (blue) catalysts. Current-step polarization curves at 700°C before (black) and after (blue) long-term operation for (b) LSM/SDCN and (c) SDCN/SDCN.

(d) OCV (red), ohmic impedance (black) and electrode polarization impedance (blue) recorded during long-term testing for LSM/SDCN (closed symbols) and SDCN/SDCN (open symbols).

The polarization behavior before and after long-term operation are shown in Figure 5b-c. For both cells, the OCV is relatively stable and degradation is clearly dominated by increasing cell area-specific resistance (ASR). The LSM/SDCN cell also shows some curvature in the polarization after operation. This is consistent with a limited increase in mass transport resistance, which may arise from the LSM densification discussed below (Figure 6). Both cells were shut off briefly at various intervals throughout operation to assess OCV and EIS spectra. The results are summarized in Figure 5d. OCV and ohmic impedance remain relatively constant throughout operation. This indicates that the seal and electrolyte hermeticity remain intact, and significant changes to the metal support, electrolyte, and electrode backbone conductivities, or catalyst electronic/ionic percolation do not occur. In contrast, the electrode polarization increases dramatically for both LSM/SDCN and SDCN/SDCN cells. This clearly indicates that stabilizing the infiltrated catalysts is the priority for ongoing work.

3.3 Post-mortem analysis

Post-mortem analysis was conducted to elucidate the causes of degradation, which was found to be dominated by increased electrode polarization as discussed above in Section 3.2. SEM images of the catalysts before and after long-term operation are shown in Figure 6. Dramatic changes to the cathode, and to a lesser extent the anode, are clearly visible. The anode catalyst evolves from a collection of ~ 20 to 50 nm particles to a denser blanket of ~100 nm features. Individual particles (light grey) are observed against a continuous background; the particles are presumed to be Ni and the background is presumed to be SDC, based on the stoichiometric ratio of each, and similarity of the particle shape to Ni particles observed in Reference [8]. Because the low Ni content (20 v%) prevents a percolating network of Ni particles, coarsening of multiple Ni particles into large micrometer-scale agglomerates with much lower surface area is not observed here. This is consistent with previous reports showing rapid degradation of

infiltrated anodes with high Ni content via coarsening [8], and mitigation of coarsening for 10 wt% Ni dispersed with co-infiltrated SDC [29]. The fresh LSM cathode catalyst is highly porous and comprised of fine discrete ~40 nm particles. After 1217 h operation, the LSM has become a much denser blanket with a rough surface with 50-100 nm features. This significant coarsening of the LSM structure is accompanied by dramatic Cr deposition, observed as light grey angular crystals on the surface of the LSM. Similar coarsening and Cr deposition is observed for the SDCN cathode after operation. Lower magnification images showing the widespread extent of Cr deposition in both cathodes are shown in the Supplementary Information (Figure S7). EDS was used to quantify the extent of Cr deposition near the cathode/electrolyte interface. No Cr was observed in the fresh cell, but peak height ratios of 2.7 Cr/La and 2.1 Cr/Ce were observed for the LSM and SDCN cathode, respectively, after ~1200 h long-term operation. For comparison, the LSM/SDCN cell operated for 300 h at 750°C had a Cr/La ratio of 2.2. Cr deposition is clearly accelerated at 750°C relative to 700°C, and we suspect this is the reason for the rapid degradation observed at 750°C (Fig 5). Based on these observations, it appears both Cr-poisoning and catalyst coarsening are key degradation mechanisms. It is not clear which dominates, but the known low tolerance of LSM to Cr poisoning suggests this is a primary degradation mode [30]. The degradation observed here is also significantly faster than observed for a metal-supported cell which similarly had infiltrated SDCN anode catalyst, but metal support only on the anode side [29]. The cathode in that work was a conventional screen-printed LSCF/CGO composite, and the current collector was Pt mesh, so Cr contamination was avoided, further supporting the conclusion that Cr deposition dominates the cells operated here. Based on these results, mitigation of Cr poisoning and catalyst coarsening is a focus of future work.

EDS observations near the stainless steel/seal interfaces indicated that elements from the seal (comprised primarily of Al, Ba, Ca oxides) did not migrate away from the seal onto the cell area for either the anode or cathode side. Significant Cr deposition on the cathode side of the seal near the stainless steel/seal interface was observed. A yellow-green color was noticed on the seal, and EDS revealed large areas of

(Ba,Cr)-oxide. This is consistent with previous work that reported yellow $BaCrO_4$ formation on the air side of a barium-calcium-aluminosilicate glass in contact with ferritic 446 stainless steel, and discussed reaction pathways including solid-state diffusion and interaction of the glass with Cr vapor [31]. The toxicity of barium chromate and depletion of Ba from the sealing glass suggest that a different seal composition may be required for commercial deployment in a MS-SOFC product.

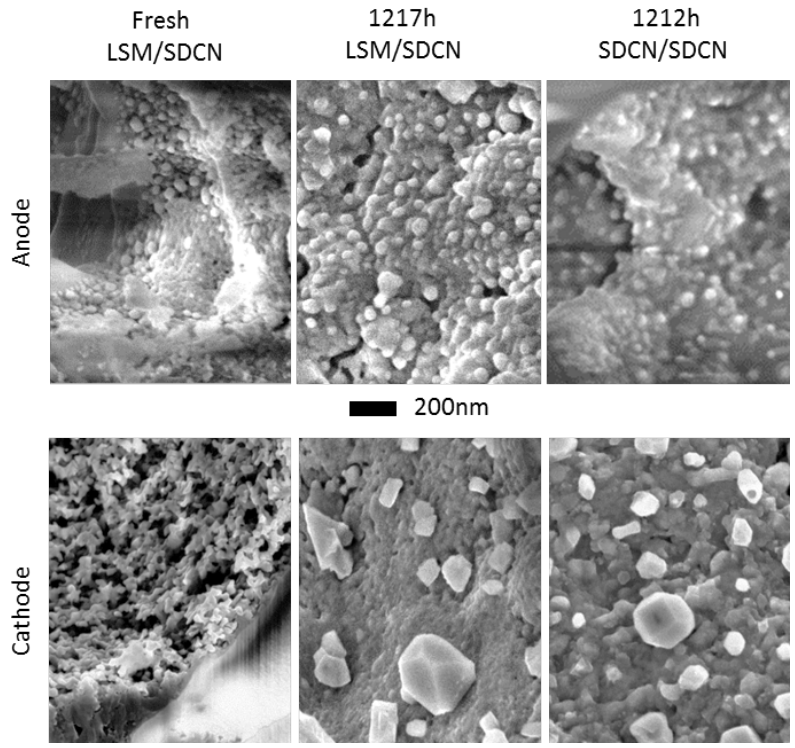

Figure 6. Impact of long-term operation on catalysts. SEM images of anode (top row) and cathode (bottom row) in the fresh state immediately after anode reduction by hydrogen at 700°C and after long-term operation.

EDS was used to estimate Cr-scale thickness on the metal support. A typical linescan near the edge of the metal in the LSM-coated cathode area is shown in Figure 7. The Cr-scale is about 0.9 μm thick. Similar scale thicknesses were observed for bare, LSM-coated, and SDCN-coated areas of the metal, for both the

LSM/SDCN and symmetric SDCN/SDCN cells tested for ~1200 h. As discussed in the Supplementary Information, assuming the observed scale growth rate persists throughout longer device lifetimes, an operation time of approximately 30,000h is required to reach a 5 μm thick scale, where spallation and concomitant loss of electrical contact is expected to occur. Clearly, Cr scale growth does not limit lifetime of the cell under the operation conditions used and degradation rates observed here.

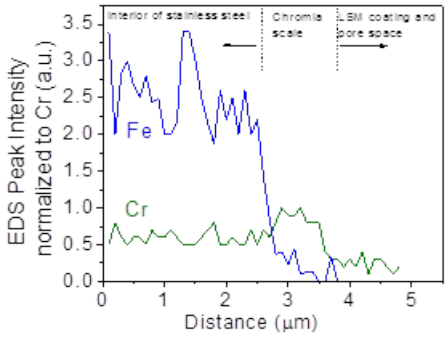

Figure 7. Chromia scale growth during long-term operation. EDS linescan of Fe (blue) and Cr (green) content of polished cross-section of cathode-side metal support of LSM/SDCN cell after 1217 h operation at 700°C.

4. Summary

Symmetric-architecture metal-supported solid oxide fuel cells were fabricated with infiltrated catalysts on both anode and cathode side. A sealing glass, GM31107, appropriate for demonstration of thermal and redox cycling, and long-term operation was selected after screening many candidate seal compositions. The seal reacted with Cr from the stainless steel support to form $BaCrO_4$, but otherwise the seal was acceptable for the purposes of demonstrating cell performance and assessing durability. LSM/SDCN cells were subjected to 200 very fast thermal cycles and 20 complete redox cycles, with minimal impact to cell performance. LSM/SDCN and SDCN/SDCN cells were operated for ~1200 h at 700°C. Significant

degradation occurred, and over the initial 500 h of operation, the degradation of the LSM/SDCN cell was faster than for the SDCN/SDCN cell. In-operando EIS and post-mortem SEM/EDS analysis suggest that catalyst coarsening and cathode Cr deposition are the dominant degradation modes. It is shown that the symmetric cell structure used here, and in particular the use of fine infiltrated catalysts and the intimate contact between the metal support and active cathode layer, causes faster degradation than observed in the literature for other metal-supported architectures. Improving catalyst stability is a focus of future work, so as to retain the advantages of the symmetric cell architecture utilized here while mitigating rapid degradation.

Acknowledgements

The author acknowledges Grace Lau for assistance with sintering and infiltrating some cells used in this work, and Sumanjeet Kaur for assistance with SEM imaging. Funding for this work was provided by Nissan Motor Co., Ltd. through Strategic Partnership Projects Agreement FP00004436. This work was funded in part by the U.S. Department of Energy under contract no. DE-AC02-05CH11231.

References

[1] M.C. Tucker, Progress in metal-supported solid oxide fuel cells: A review, J. Power Sources. 195 (2010) 4570–4582. doi:10.1016/j.jpowsour.2010.02.035.

[2] Y. Larring, M.-L. Fontaine, Critical Issues of Metal-Supported Fuel Cell, Green Energy Technol. 55 (2013). doi:10.1007/978-1-4471-4456-4.

[3] A.M. Dayaghi, K.J. Kim, S.J. Kim, J. Park, S.J. Kim, B.H. Park, G.M. Choi, Stainless steel-supported solid oxide fuel cell with La0.2Sr0.8Ti0.9Ni0.1O3−δ/yttria-stabilized zirconia composite anode, J. Power Sources. 324 (2016) 288–293. doi:10.1016/j.jpowsour.2016.05.076.

[4] and H.-P.B. Th. Franco, M. Haydn, A. Weber, W. Schafbauer, L. Blum, U. Packbier, D. Roehrens, N.H. Menzler, J. Rechberger, A. Venskutonis, L. S. Sigl, The status of metal-supported

SOFC development and industrialization at Plansee Th. Franco, ECS Trans. 57 (2013) 471–480. doi:10.1149/05701.0471ecst.

[5] V.V. Krishnan, Recent developments in metal-supported solid oxide fuel cells, Wiley Interdiscip. Rev. Energy Environ. (2017) e246. doi:10.1002/wene.246.

[6] J. Harris, Y. Yan, R. Bateni, O. Kesler, Degradation of $La_{0.6}Sr_{0.4}Co_{0.2}Fe_{0.8}O_{3-\delta}$-$Ce_{0.8}Sm_{0.2}O_{1.9}$ Cathodes on Coated and Uncoated Porous Metal Supports, Fuel Cells. (2016) 1–11. doi:10.1002/fuce.201500139.

[7] E.S.C. Fan, J. Kuhn, O. Kesler, Suspension plasma spraying of La0.6Sr0.4Co0.2Fe0.8O3-?? cathodes: Influence of carbon black pore former on performance and degradation, J. Power Sources. 316 (2016) 72–84. doi:10.1016/j.jpowsour.2016.02.075.

[8] M.C. Tucker, G.Y. Lau, C.P. Jacobson, L.C. DeJonghe, S.J. Visco, Stability and robustness of metal-supported SOFCs, J. Power Sources. 175 (2008) 447–451. doi:10.1016/j.jpowsour.2007.09.032.

[9] M.C. Tucker, Development of High Power Density Metal-Supported Solid Oxide Fuel Cells, Energy Technol. (2017).

[10] M.C. Tucker, G.Y. Lau, C.P. Jacobson, L.C. DeJonghe, S.J. Visco, Performance of metal-supported SOFCs with infiltrated electrodes, J. Power Sources. 171 (2007) 477–482. doi:10.1016/j.jpowsour.2007.06.076.

[11] M.C. Tucker, A.S. Ying, Metal-Supported Solid Oxide Fuel Cells Operated in Direct-Flame Configuration, J. Power Sources. (2017).

[12] M. Tucker, B. Carreon, J. Charyasatit, K. Langston, C. Taylor, J. Manjarrez, N. Burton, M. Labarbera, C.P. Jacobson, R&D and Commercialization of Metal-Supported SOFC Personal Power Products at Point Source Power, ECS Trans. 57 (2013) 503–509.

[13] M.C. Tucker, C. Taylor, M. LaBarbera, C.P. Jacobson, Operation of Metal-Supported SOFC with Charcoal Fuel, ECS Trans. 57 (2013) 2929–2937.

[14] M. Tucker, B. Carreon, J. Charyasatit, K. Langston, C. Taylor, J. Manjarrez, N. Burton, M.

Labarbera, C.P. Jacobson, Playing with Fire: Commercialization of a Metal-Supported SOFC Product for Use in Charcoal Cookstoves for the Developing World, ECS Trans. (2017).

[15] J.C. Ruiz-Morales, D. Marrero-López, J. Canales-Vázquez, J.T.S. Irvine, Symmetric and reversible solid oxide fuel cells, RSC Adv. 1 (2011) 1403. doi:10.1039/c1ra00284h.

[16] J. Zhou, T.-H. Shin, C. Ni, G. Chen, K. Wu, Y. Cheng, J.T.S. Irvine, In situ Growth of Nanoparticles in Layered Perovskite La0.8Sr1.2Fe0.9Co0.1O4-δ as an Active and Stable Electrode for Symmetrical Solid Oxide Fuel Cells, Chem. Mater. (2016) acs.chemmater.6b00071. doi:10.1021/acs.chemmater.6b00071.

[17] T. Klemensø, J. Nielsen, P. Blennow, Å.H. Persson, T. Stegk, B. Holl, S. Sønderby, High performance metal-supported solid oxide fuel cells with Gd-doped ceria barrier layers, 196 (2011) 9459–9466. doi:10.1016/j.jpowsour.2011.07.014.

[18] P. Szabo, J. Arnold, T. Franco, M. Gindrat, A. Refke, A. Zagst, A. Ansar, Progress in the Metal Supported Solid Oxide Fuel Cells and Stacks for APU, ECS Trans. 25 (2009) 175–185.

[19] P. Bance, N.P. Brandon, B. Girvan, P. Holbeche, S.O. Dea, B.C.H. Steele, Spinning-out a fuel cell company from a UK University — 2 years of progress at Ceres Power, 131 (2004) 86–90. doi:10.1016/j.jpowsour.2003.11.077.

[20] Y. Zhou, X. Ye, J. Li, Z. Zhan, S. Wang, Metal-Supported Solid Oxide Fuel Cells with a Simple Structure, J. Electrochem. Soc. 161 (2014) F332–F336. doi:10.1149/2.085403jes.

[21] T.Z. Sholklapper, V. Radmilovic, C.P. Jacobson, S.J. Visco, L.C. De Jonghe, Synthesis and Stability of a Nanoparticle-Infiltrated Solid Oxide Fuel Cell Electrode, Electrochem. Solid-State Lett. 10 (2007) B74–B76. doi:10.1149/1.2434203.

[22] M.C. Tucker, Metal-Supported Solid Oxide Fuel Cell With High Power Density, ECS Trans. (2017).

[23] B.J. Ingram, T.A. Cruse, M. Krumpelt, Potassium-assisted chromium transport in solid oxide fuel cells, J. Electrochem. Soc. 154 (2007) B1200–B1205. doi:10.1149/1.2781117.

[24] M.C. Tucker, C.P. Jacobson, L.C. De Jonghe, S.J. Visco, A braze system for sealing metal-

supported solid oxide fuel cells, J. Power Sources. 160 (2006) 1049–1057. doi:10.1016/j.jpowsour.2006.02.067.

[25] U. Bossel, Rapid startup SOFC modules, Energy Procedia. 28 (2012) 48–56. doi:10.1016/j.egypro.2012.08.039.

[26] L.M. Rodriguez-Martinez, L. Otaegi, M.A. Alvarez, M. Rivas, N. Gomez, A. Zabala, N. Arizmendiarrieta, I. Antepara, A. Urriolabeitia, I. Villarreal, A. Laresgoiti, Degradation Studies on Tubular Metal Supported SOFC, ECS Trans. 25 (2009) 745–752.

[27] A.M. Dayaghi, K.J. Kim, S.J. Kim, S. Kim, H. Bae, G.M. Choi, Thermal cycling and electrochemical characteristics of solid oxide fuel cell supported on stainless steel with a new 3-phase composite anode, J. Power Sources. 354 (2017) 74–84. doi:10.1016/j.jpowsour.2017.04.022.

[28] D. Sarantaridis, R.A. Rudkin, A. Atkinson, Oxidation failure modes of anode-supported solid oxide fuel cells, J. Power Sources. 180 (2008) 704–710. doi:10.1016/j.jpowsour.2008.03.011.

[29] P. Blennow, J. Hjelm, T. Klemens??, S. Ramousse, A. Kromp, A. Leonide, A. Weber, Manufacturing and characterization of metal-supported solid oxide fuel cells, J. Power Sources. 196 (2011) 7117–7125. doi:10.1016/j.jpowsour.2010.08.088.

[30] S.P. Jiang, X. Chen, Chromium deposition and poisoning of cathodes of solid oxide fuel cells - A review, Int. J. Hydrogen Energy. 39 (2014) 505–531. doi:10.1016/j.ijhydene.2013.10.042.

[31] Z. Yang, K.D. Meinhardt, J.W. Stevenson, Chemical Compatibility of Barium-Calcium-Aluminosilicate-Based Sealing Glasses with the Ferritic Stainless Steel Interconnect in SOFCs, (2003) 1095–1101. doi:10.1149/1.1590325.

Figure Captions

Figure 1. SEM image of (a,b) polished cross section of MS-SOFC structure after sintering and before catalyst infiltration, and (c) cathode pore after infiltration of LSM. Reproduced with permission from Ref. 9.

Figure 2. Rapid thermal cycling of LSM/SDCN cell. Temperature history for (a) several cycles and (b) a single heat-up. (c) Cell OCV (open symbols) and peak power density (closed symbols) at 700°C during repeated thermal cycling.

Figure 3. Deep redox cycling of LSM/SDCN cell. Cell OCV (open symbols) and peak power density (closed symbols) at 700°C during repeated air/hydrogen redox cycling of the anode.

Figure 4. Temperature-dependence of the initial cell stability of LSM/SDCN cell. (a) Current density at 0.7 V and (b) OCV for cells operated potentiostatically at 650°C (blue), 700°C (black) and 750°C (red).

Figure 5. Long-term operation. (a) Current density at 0.7 V for cells operated potentiostatically at 700°C with LSM/SDCN (black) and symmetric SDCN/SDCN (blue) catalysts. Current-step polarization curves at 700°C before (black) and after (blue) long-term operation for (b) LSM/SDCN and (c) SDCN/SDCN. (d) OCV (red), ohmic impedance (black) and electrode polarization impedance (blue) recorded during long-term testing for LSM/SDCN (closed symbols) and SDCN/SDCN (open symbols).

Figure 6. Impact of long-term operation on catalysts. SEM images of anode (top row) and cathode (bottom row) in the fresh state immediately after anode reduction by hydrogen at 700°C and after long-term operation.

Figure 7. Chromia scale growth during long-term operation. EDS linescan of Fe (blue) and Cr (green) content of polished cross-section of cathode-side metal support of LSM/SDCN cell after 1217 h operation at 700°C.